Co-published by
Institute of Fluid-Flow Machinery
Polish Academy of Sciences
Committee on Thermodynamics and Combustion
Polish Academy of Sciences

Copyright©2026 by the Authors under licence CC BY-NC-ND 4.0

http://www.imp.gda.pl/archives-of-thermodynamics/

Experimental validation of the CFD model of heat losses from the horizontal rectangular flue gas duct exposed to wind and solar radiation

Liliana Mirosz

Warsaw University of Technology, Department of District Heating and Gas Systems, Faculty of Environmental Engineering, Nowowiejska 20, Warsaw 00-653, Poland
Author email: liliana.mirosz@pw.edu.pl

Received: 29.09.2025; revised: 28.04.2026; accepted: 12.06.2026

Abstract

The article presents the experimental validation of a numerical model of heat losses from a horizontal rectangular flue gas duct situated outside a heating plant building. The duct is insulated with mineral wool mats and protected with galvanised sheet metal. The model was developed in ANSYS Fluent 2024 R2, incorporating the effects of wind velocity and solar radiation. The computational domain is defined as encompassing the duct and the surrounding airspace. A sensitivity analysis of the mesh on the simulation results was performed. The validation experiment was conducted at an operational coal-fired heating plant under various wind and sunlight conditions. The measurement of the heat flux density was conducted by means of heat flux sensors. The validation indicators, that is to say, the process validation metric and the relative root mean square error, confirm the consistency between the simulation results and the heat flux density measurements on the bottom and side walls. The numerical model that has been utilised is capable of being employed in analyses of flue gas duct modernisation, with the objective of reducing heat losses from flue gases flowing through the duct.

Keywords: Computational fluid dynamics; Heat losses; Rectangular flue gas duct; Solar radiation; Thermal insulation

Vol. 47(2026), No. 3, 173–186; doi: 10.24425/ather.2026.7516

Cite this manuscript as: Mirosz, L. (2026). Experimental validation of the CFD model of heat losses from the horizontal rectangular flue gas duct exposed to wind and solar radiation. *Archives of Thermodynamics*, 47(3), 173–186.

1. Introduction

Statistics Poland [1] have reported that in 2024, district heating was utilised for the heating of 45% of households in Poland. This share is so large that even a negligible enhancement in the energy efficiency of heat generation has the potential to markedly diminish the environmental impact of heat production in residential buildings. According to data from the Energy Regulatory Office [2], the average efficiency of licensed sources was 84% in 2024, representing a 5pp increase since 2002. The efficiency level is determined by the magnitude of various heat losses that occur in the process of heat production. For coal-fired heating plants, the following factors warrant consideration: exhaust heat loss carried by flue gases into the environment, incomplete combustion loss caused by the presence of combustible particles in fly ash and slag, heat losses to the environment through convection and radiation, physical heat contained in combustion residues (the so-called physical enthalpy of residues), and incomplete combustion loss resulting from the partial combustion of gaseous combustible components in flue gases. Figure 1 shows examples of the shares of these heat losses for a coal-fired water boiler.

Nomenclature

a_1 – model constant
CV(RMSE)– relative root mean square error coefficient, %
c_p – specific heat capacity at constant pressure, J/(kg K)
D – measured value
D_ω – cross-diffusion term, kg/(m^3 s^2)
d – hydraulic diameter, m
e – error, %
E – comparison error
F_1, F_2– first and second blending functions
G – energy production, kg/(m/s^3)
GCI – grid convergence index, %
Gr – Grashof number
g – gravitational force, m/s^2
h – characteristic cell size, m
H – height, m
I – turbulence intensity, %
k – kinetic energy of turbulence, m^2/s^2
Ma – Mach number
n – number of measurements in a series
N – number of grid cells
p – pressure, Pa
p_{conv} – order of convergence
Q – heat flux density, W/m^2
r – grid refinement ratio
Re – Reynolds number
RMSE– root mean square error
s – standard deviation
S – modulus of the mean rate-of-strain tensor, 1/s
S_{num} – numerical simulation value
t – temperature, ^{o}C
t_p – Student's t-distribution coefficient for confidence level p
T – absolute temperature, K
u_a – type A standard uncertainty
u_b – systematic standard uncertainty
u_c – combined standard uncertainty
U – uncertainty
U_V – process validation metric
V – computational domain volume, m^3
$\boldsymbol{w}$ – velocity vector, m/s
w_x – velocity component in the x-axis direction, m/s
x – segment length in x-axis direction, m
y^+ – dimensionless wall distance in turbulence models

Greek symbols

α^* – coefficient damping the turbulent viscosity
β^* – modified dissipation coefficient for k
β_i – blended dissipation coefficient for ω
γ_1 – production coefficient for ω
δ – thickness, m
λ – thermal conductivity, W/(m K)
μ – dynamic viscosity, $\mu = \rho k/\omega$, kg/(m s)
μ_t – turbulent viscosity, kg/(m s)
ν – kinematic viscosity, m^2/s
ν_{dof} – number of degrees of freedom
ρ – density, kg/m^3
σ – diffusion coefficient
ω – turbulence dissipation rate, 1/s

Subscripts and Superscripts

a – relative
c – total
D – experimental value
ext – extrapolated
i – measurement number in a series
k – turbulent kinetic energy
SN – numerical simulation value
SPD – due to input data
t – turbulent
x – coordinate direction
v – viscous sublayer
ω – turbulence dissipation rate
1 – for wall layers
2 – for the region far from the wall
‘ – fluctuation of a variable

Abbreviations and Acronyms

CFD – computational fluid dynamics
GCI – grid convergence index

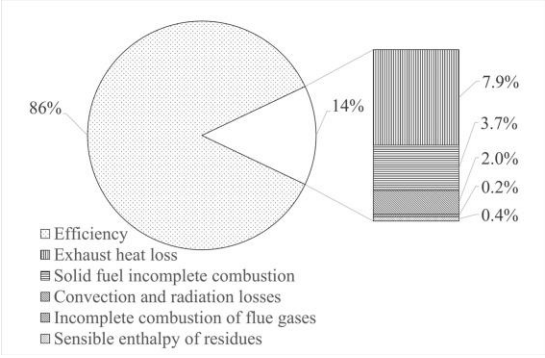


Fig. 1. Shares of heat losses for an example coal-fired water boiler (own study based on [3]).

In the case of a boiler that is operated in accordance with the established guidelines, exhaust loss constitutes the most significant element in its energy balance. As Zhang et al. [3] assert, this may account for as much as 8–9% in the case of coal-fired water boilers, a subject to be analysed later in this article. This phenomenon of heat losses can be mitigated through various means, including the reduction of flue gas temperature, with due consideration for the issue of sulphur corrosion on the walls of both horizontal and vertical flue gas ducts. The conditions for its occurrence are associated with the location of the ducts, which, in the context of heating plants, are partially situated outside the building. Subsequently, the flue gas is exposed to meteorological conditions, including wind and precipitation, which prompt a rapid cooling process. It is imperative to maintain the temperature of the flue gas above the so-called acid dew point, where the mixture of sulfuric acid and water vapour condenses, leading to the corrosion of ducts. Consequently, proper insulation of the flue gas discharge route, and even at the design stage, the optimal route for reducing heat loss, is a factor that significantly affects the efficiency of district heating production.

It is evident that a considerable number of heating plants and combined heat and power plants are currently in operation in Poland. It is important to note that many of these facilities were constructed several decades ago. The modernisation of existing flue gas ducts has been demonstrated to result in a substantial enhancement of the efficiency of district heating production. The magnitude of this increase can be estimated using numerical simulations, provided that the extent to which they reflect reality is known. The validation of numerical models of flue gas flows in heating plants by comparing simulation results with measurements on actual facilities is a subject that is rarely described in the literature. The primary rationale for this is the complexity inherent in such studies, which is compounded by the extensive scale of the model and frequently necessitates disruption to the existing installation.

A review of the extant literature reveals a paucity of research on the validation of numerical models for a horizontal rectangular section of flue gas ducts based on measured heat flux density. Nevertheless, there are a number of publications that address this topic in specific areas.

Matas et al. [4] and Chen et al. [5] described the issue of a rectangular horizontal section of a flue gas duct, focusing on flow velocities. Matas et al. [4] validated a numerical model of the flue gas system between the boiler and the fan by comparing the simulation results with measurement data obtained at a combined heat and power plant. The model under consideration incorporated short rectangular horizontal sections. It was determined that the correspondence between the simulation outcomes and the measurement data was deemed to be satisfactory, as evidenced by the findings concerning the flue gas flow rates and velocity distribution. Chen et al. [5] presented an analysis of the numerical simulation results for a rectangular flue gas duct, examining the conditions upstream and downstream of an electrostatic precipitator. The velocity distribution was also described. The publication did not include any validation.

Conversely, El-Shafie [6] utilised temperature measurements to validate a numerical model, albeit for a vertical circular flue gas duct discharging flue gas from a glass furnace. The demonstration revealed a substantial degree of concordance between the temperature distribution that was derived from the numerical simulation and the measurement results.

None of the above publications takes into account the current influence of wind. None of the numerical models presented cover the air around the flue gas duct. Nevertheless, this approach is frequently employed in numerical simulations of flows around buildings, as articulated by Huang et al. [7]. The literature provides comprehensive guidelines for the numerical simulation and validation of numerical models of buildings, with consideration for external air flow (see, for example, Franke et al. [8], Tominaga et al. [9]). Outside the boiler room building, the flue gas duct is significantly affected by the external air. Consequently, it appears that, in numerical simulations, it could be treated in the same way as a building.

It has been observed that the aforementioned publications neglect to consider the impact of solar radiation, a factor that is undoubtedly implicated in the intensity of heat exchange between the flue gases and the environment.

The present work serves to augment the extant body of knowledge concerning the impact of outside air and solar radiation on heat losses from flue gas ducts. The objective of this study is to utilise numerical simulations to formulate solutions that enhance the efficiency of district heating production by reducing heat losses from flue gas ducts.

2. Numerical model of heat losses from the flue gas duct of a heating plant

2.1. Fundamental equations of conservation

Computational fluid dynamics (CFD) is a technique for solving problems involving fluid flow and the accompanying heat exchange using numerical methods. It is imperative that these solutions adhere to the established laws of conservation in the physics of the phenomenon. It is imperative to acknowledge the fundamental principle of fluid mechanics: the conservation of mass. In accordance with Newton's second law of motion, the change in momentum of a fluid particle must be equal to the sum of the forces acting upon it. In accordance with Newton's first law of motion, the change in energy must be equal to the sum of the changes in heat transfer and the changes in work done on the fluid element.

The law of conservation of mass gives rise to the continuity equation described in Eq. (1), under the assumption that the phenomenon is steady-state. The numerical model investigated in this study involves two fluids: flue gas and air. Both are assumed to be incompressible with respect to pressure changes, as the Mach number remains below 0.3. While flue gas is also considered incompressible with respect to thermally induced density changes, due to the dominance of forced convection within the duct, air is treated as thermally compressible. This approach is necessary to model the mixed convection around the duct, which is key to capturing buoyancy effects caused by flow separation as the wind encounters the structure. Equation (1) represents the continuity equation for both fluids

$$\nabla \cdot (\rho \boldsymbol{w}) = 0, \tag{1}$$

where: ρ – density, $\boldsymbol{w}$ – velocity vector. In the case of flue gas, the density is assumed constant, whereas for air, it varies according to the thermal compressibility assumption.

The law of momentum change is described by the momentum conservation equation. This work presents its averaged version, i.e. the Reynolds equation described in Eq. (2). The velocity component in the *x*-axis direction is given. In addition to the aforementioned assumptions, the fluid flow is turbulent, and gravity is taken into account in the *x*-axis direction, with the opposite sign:

$$\nabla \cdot (\rho \boldsymbol{w} w_x) = -\frac{\partial p}{\partial x} + \nabla \cdot (\mu \nabla w_x) - \nabla \cdot \left(\rho \overline{w_x{}' \boldsymbol{w}'}\right) - \rho g, \tag{2}$$

where: w – velocity, p - pressure, x – segment length in the x-axis direction, μ – dynamic viscosity, g – gravitational acceleration, and other quantities as indicated in Eq. (1). The subscript x denotes the vector component in the x-axis direction, and ’ denotes fluctuations of variables. Analogous equations describe the conservation of momentum’ in the other directions.

In the analysed phenomenon of heat exchange between flue gas and air, the influence of gravity on the flow from the flue gas side is negligible. However, this is not the case on the air side. The phenomenon of mixed convection can be defined as a combination of free convection, which is influenced by temperature differences and affects density, and forced convection, which is driven by the action of wind. In order to estimate the influence of gravity, the ratio of the Grashof number to the square of the Reynolds number was calculated for the measurement from the experiment at the highest wind velocity. The result obtained was 0.04, which, according to Bejan [10], indicates a small but not negligible influence of buoyancy forces on air density. It is important to note that this effect will increase as the wind velocity decreases. It is therefore evident that all simulations were performed with due consideration for gravitational forces.

The governing law of energy changes is regulated by the energy conservation equation, as outlined in Eq. (3). Along with the previously stated assumptions, there are no internal heat sources, and energy dissipation due to working against viscous forces can be neglected:

$$\nabla \cdot \left(\rho c_p \boldsymbol{w} T\right) = \nabla \cdot (\lambda \nabla T) - \nabla \cdot \left(\rho c_p \overline{\boldsymbol{w}' T'}\right), \tag{3}$$

where: c_p – specific heat capacity at constant pressure, T – absolute temperature, λ – thermal conductivity.

2.2. Turbulence model

The phenomenon of heat exchange in the flue gas duct was modelled using the software programme ANSYS Fluent 2024 R2. It is widely used in numerical simulations of flows around buildings that take into account the influence of external air velocity, as described by Huang et al. [7].

In the analysed case, turbulent motion occurs on both the flue and air sides. In the proximity of the walls, the nature of the flow undergoes a transformation. In order to achieve a reliable representation of the flow field within a reasonable computational time, appropriate turbulence models are selected. It is posited that these models provide a reliable approximation of the effect of turbulence on the average velocity, pressure and temperature fields. This enables accurate and stable calculation results to be obtained with an acceptable computational effort.

In the aforementioned issue, the Reynolds-averaged Navier-Stokes (RANS) model was selected, in which all vortex scales are modelled, the so-called Shear-Stress Transport (SST k–ω). This model has been employed in analogous analyses within the extant literature (see, for example, Matas et al. [4]). The model demonstrates an effective solution to the equations in the wall layer at low speeds. In the fully turbulent area far from the wall, the k–ε model is employed. Hamisu et al. [11] posit that the recommended value of y^+ for the SST k–ω model is approximately 1, although values up to 5 are deemed acceptable.

The phenomenon of turbulence is taken into account in CFD in the k–ω SST model by solving the equations of kinetic energy transport of turbulence and turbulence dissipation rate, respectively:

$$\nabla \cdot (\rho k \boldsymbol{w}) = \nabla \cdot [(\mu + \mu_t \sigma_k) \nabla k] + G_k - \rho \beta^* \omega k, \tag{4}$$

$$\nabla \cdot (\rho \omega \boldsymbol{w}) = \nabla \cdot [(\mu + \mu_t \sigma_\omega) \nabla \omega] + \gamma_1 \frac{\omega}{k} G_k - \rho \beta_i \omega^2 + D_\omega. \tag{5}$$

The model also incorporates a specific formulation for turbulent viscosity, a blended dissipation coefficient and a cross-diffusion term, respectively:

$$\mu_t = \frac{\rho k}{\omega} \frac{1}{\max\left[\frac{1}{\alpha^*}, \frac{SF_2}{a_1 \omega}\right]}, \tag{6}$$

$$\beta_i = F_1 \beta_{i,1} + (1 - F_1) \beta_{i,2}, \tag{7}$$

$$D_\omega = 2(1 - F_1) \rho \sigma_{\omega,2} \frac{1}{\omega} \nabla k \cdot \nabla \omega, \tag{8}$$

where: k – turbulent kinetic energy, μ_t – turbulent viscosity, σ_k, σ_ω – diffusion coefficients both equal to 0.5 in wall layers, and equal to 1.0 and 0.856 ($\sigma_{\omega,2}$) far from the walls, respectively, G_k – production of turbulent kinetic energy, β^* – modified dissipation coefficient for k equal to 0.09, ω – specific dissipation rate, γ_1 – production coefficient for ω equal to 0.52 for high-Reynolds number flows, β_i – blended dissipation coefficient for ω, D_ω – cross-diffusion term, α^* – coefficient damping the turbulent viscosity equal to 1 for high-Reynolds number flows, S – modulus of the mean rate-of-strain tensor, F_1, F_2 – first and second blending functions, a_1 – model constant equal to 0.31, $\beta_{i,1}$, $\beta_{i,2}$ – dissipation coefficients for ω equal to 0.075 in wall layers and 0.0828 far from the walls, respectively.

The mathematical formulation follows the original notation proposed by Menter [12], while coefficients and model implementation are based on the ANSYS Fluent documentation [13]. It was assumed that the flue gas is incompressible with respect to both pressure and temperature changes. In contrast, air was modelled as incompressible regarding pressure but thermally compressible, as described in Subsection 2.1. The phenomenon is assumed to be steady-state, and no internal heat sources are present.

2.3. Solar radiation model

In order to account for the impact of solar radiation on the flue gas duct, the Solar Load Model in ANSYS Fluent 2024 R2 was utilised. In this model, the impact of solar radiation is determined on the basis of three factors. Firstly, data on the location of the actual installation must be taken into account. Secondly, the date of the measurement series must be considered. Thirdly, the solar radiation coefficient must be taken into account. The solar radiation coefficient was calculated on the basis of the air temperature measured in conditions of shade and in the sun during the measurement series in the validation experiment. For the measurement series for which a cloudless sky was observed, this coefficient was assumed to be equal to 1. This corresponds to the difference in air temperature between the measurement in the shade and in direct sunlight, as measured at that time. For the remaining measurement series, the insolation coefficient was calculated in relation to the above-mentioned measurement series, based on the current difference in air temperature measured in the shade and in direct sunlight.

The absorptivity of the duct walls, ground (predominantly grass) and building envelope was assumed to be 0.8, accounting for material properties, ageing, and coal dust deposition typical

of the coal-fired heating plant environment. Carvalho et al. [14] reported an albedo of 0.25 for grass corresponding to an absorption coefficient of 0.75. In this study, the absorption coefficient was increased to 0.8 to reflect the significant darkening of vegetation caused by coal dust accumulation. Similarly, the building envelope's absorptivity was based on Yu et al. [15], who identified a range of 0.65 – 0.85 for grey wall-facing materials. The value of 0.8 was selected due to long-term environmental exposure. For blue-painted steel ducts, the baseline from Liu et al. [16] (0.63–0.75 for grey coatings) was adjusted to 0.8. This adjustment accounts for the higher near-infrared absorption typical of standard blue pigments compared to grey ones, as well as the further increase in absorptivity caused by coal dust contamination.

While ANSYS Fluent also allows for radiation exchange calculations between surfaces and gases, the Radiation Model was not activated for two main reasons. First, at the investigated temperatures (below 400 K for flue gas, and below 300 K for air), gases are generally considered transparent [17]. Furthermore, since radiant energy emission is proportional to the fourth power of absolute temperature, its contribution at these moderate temperatures is negligible compared to convective fluxes observed in this study. Consequently, omitting the radiation model does not significantly impact the final results.

2.4. Geometry of the computational domain

The geometry of the model was created in ANSYS DesignModeler. The issue was regarded as a three-dimensional problem. The modelled geometry is shown in Fig. 2:

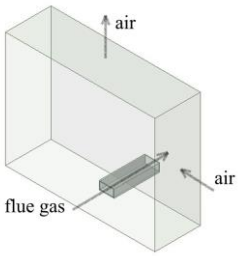


Fig. 2. Geometric model showing the direction of flue gas and air flows (ANSYS DesignModeler 2024 R2).

The duct in question was modelled with a thickness of 4 mm, with the material used being steel sheet. The duct insulation is composed of two mineral wool mats, each measuring 50 mm in thickness, which are sheathed in 0.5 mm-thick galvanised sheet metal. The duct exhibits a rectangular cross-section, with the following internal dimensions: width of 2.12 m, height of 1.06 m, length of 7.04 m. The geometry of the model is such that it takes into account the volume of the duct and the insulation. The sheets were modelled as surfaces with thicknesses assigned in ANSYS Fluent 2024 R2.

The direction of flow of flue gas and the direction of air inlet are perpendicular to each other. The location of the air outlet is above rather than behind the duct. This is due to the proximity of a building, which blocks the flow. The dimensions of the computational domain, in the absence of guidelines for flue ducts, were based on guidelines for modelling wind flow around buildings, presented by Franke et al. [8] and Tominaga et al. [9]. The domain extends 10H above the duct, while a distance of 5H was modelled between the wind inlet plane and the duct, where H is the height of the duct. The selection of these values was informed by a blockage ratio of 7%. This ratio is utilised to ascertain the distances between the wind inlet and outlet, and the object around which the wind flows. The ratio is defined as the cross-sectional area of the obstacle (in this case, the channel) divided by the cross-sectional area of the air domain in the direction of air inflow. The location of the installation was a determining factor in the dimensions of the air domain: 11.5H behind the channel (building boundary) and 4 m below the channel (ground level). The width of the computational domain was assumed to be equal to the length of the analysed section.

2.5. Discretisation of the computational domain

The spatial discretisation of the computational domain performed in ANSYS ICEM CFD 2024 R2 is presented in Fig. 3.

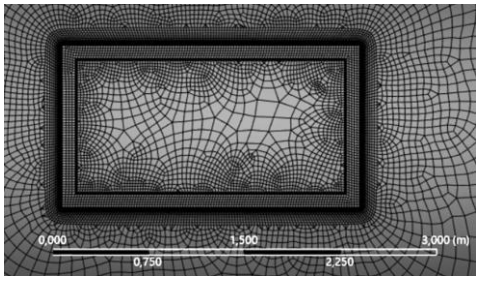


Fig. 3. Numerical mesh: view from the flue gas inlet toward the duct (ANSYS ICEM CFD 2024 R2).

The limit for the minimum cell size in the fully turbulent area on the air side was assumed based on the cube root of the duct volume, i.e. 0.27 m, in accordance with the guidelines for buildings provided by Franke et al. [8].

The mesh was refined near the duct walls in order to rectify the issue of heat transfer in the wall layers. These are the layers, in which the fluid's viscosity is a significant factor in determining its flow. For the purpose of this study, the thickness of the aforementioned zone was estimated for flue gases based on the formula for turbulent flow through a pipe, Eq. (9), as posited by Schlichting and Gersten [18]. Such flow is divided into a viscous sublayer and a turbulent core:

$$\delta_v = 122 \frac{\ln \mathrm{Re}}{\mathrm{Re}\, \mathrm{G}(\ln \mathrm{Re})} d, \tag{9}$$

where: δ_v – thickness of the viscous sublayer of flue gas, Re – Reynolds number, and function G(ln Re) is equal to 1.35 at $2300 < \mathrm{Re} < 10^7$, and d – hydraulic diameter.

However, the thickness of the wall layer was calculated according to the formula given by Schlichting and Gersten [18] for turbulent flow along a plate:

$$\delta_t = 0.14 \frac{\mathrm{Re}}{\ln \mathrm{Re}} \mathrm{G}(\ln \mathrm{Re}) \frac{\nu}{w}, \tag{10}$$

where δ_t is the thickness of the turbulent boundary layer of air,

v is the kinematic viscosity, and function G(ln Re) is equal to 15 at $10^5 < \mathrm{Re} < 10^6$.

According to Duan et al. [19], the Reynolds number on the flue gas side was determined using the square root of the channel cross-sectional area as the characteristic dimension. On the air side, the channel width was taken as the characteristic dimension for the flow along the plate.

The thicknesses at which mesh refinement is important were calculated for the data from each measurement series. The maximum values recorded were 0.004 m on the flue gas side and 0.04 m on the air side. On this basis, the grid refinement at the walls was modelled accordingly so that it covered at least the estimated thickness of the wall zone. The layer thickness growth rate was set at 1.2, at which the independence of the grid influence on the numerical simulation result, as determined by the grid convergence index (GCI), is less than 1%. In accordance with the recommendations set out by Franke et al. [8], the maximum value for numerical simulations of wind flow around buildings, it should not exceed 1.2. The thicknesses of the first layer in the wall zone are 0.0001 m on the flue gas side and 0.0003 m on the air side, respectively. In the context of these thicknesses, the maximum values of y^+ at the walls did not exceed 5, in accordance with the recommendations for the SST k–ω turbulence model.

The simulations were executed on a grid, the independence analysis of which is presented in the following chapter. The total number of mainly hexahedral volume elements was approximately 2 million. The quality of the mesh was verified to ensure numerical stability and accuracy. The skewness reached a maximum value of 0.8 (with an average of 0.2), and the minimum orthogonal quality was 0.2 (with an average of 0.9). Although a maximum aspect ratio reached 1005 (with an average of 86 for the entire domain), these peak values occurred exclusively within the wall layers. In the computational domain far from the walls, the maximum aspect ratio remained below 6.

2.6. Mesh independence analysis

The independence of the results from the mesh used was tested using GCI. This method is frequently employed to estimate discretisation error in numerical fluid dynamics analyses, as evidenced by the works of Franke et al. [8] and Celik et al. [20]. According to Roache [21], GCI is derived from the generalised Richardson extrapolation method, which determines the numerical uncertainty associated with spatial discretisation errors. The relative error of the test of independence of results from the mesh necessitates solutions for a minimum of three grids of varying refinement. A uniform refinement in all directions was assumed between successive meshes, and the layer growth rate was modified in the wall area (changes of approximately 25%). The number of layers at the walls was adjusted to cover the estimated total thickness of the near-wall layer. In all types of grids, meticulous attention was paid to ensure adequate quality. This was achieved by analysing the aspect ratio, orthogonality and skewness of its elements. If deemed necessary, the mesh division along the flue gas duct axis was corrected.

Celik et al. [20] proposed the following methodology for calculating GCI from Eq. (11) based on the results of numerical simulations on three distinct grids, designed as follows: fine – 1, medium – 2, and coarse – 3:

$$\mathrm{GCI}_1^{21} = \frac{1.25 e_a^{21}}{r_{21}^{p_{\mathrm{conv}}-1}}, \tag{11}$$

where: e_a – relative error between the results obtained from the two meshes, r – grid refinement ratio (recommended > 1.3), p_{conv} – order of convergence.

The relative error between the results from two meshes is calculated from:

$$e_a^{21} = \left| \frac{S_{\mathrm{num},1} - S_{\mathrm{num},2}}{S_{\mathrm{num},1}} \right|, \tag{12}$$

where S_{num} stands for the numerical simulation value.

The grid refinement ratio, expressed as

$$r_{21} = \frac{h_2}{h_1} \tag{13}$$

is determined based on the characteristic cell size using the equation:

$$h_1 = \left(\frac{V}{N_1} \right)^{1/3}, \tag{14}$$

where V is the computational domain volume and N is the number of grid cells.

The order of convergence of the numerical method is determined iteratively according to the equation:

$$p_{\mathrm{conv}} = \frac{1}{\ln(r_{21})} \left| \ln \left| \frac{S_{\mathrm{num},3} - S_{\mathrm{num},2}}{S_{\mathrm{num},2} - S_{\mathrm{num},1}} \right| + \right.$$

$$\left. + \ln \left(\frac{r_{21}^{p_{\mathrm{conv}}} - \mathrm{sgn}\left(\frac{S_{\mathrm{num},3} - S_{\mathrm{num},2}}{S_{\mathrm{num},2} - S_{\mathrm{num},1}} \right)}{r_{32}^{p_{\mathrm{conv}}} - \mathrm{sgn}\left(\frac{S_{\mathrm{num},3} - S_{\mathrm{num},2}}{S_{\mathrm{num},2} - S_{\mathrm{num},1}} \right)} \right) \right|, \tag{15}$$

for which the quantities are described in the preceding formulas.

The relative error extrapolated between the results obtained from the two grids is calculated from:

$$e_{\mathrm{ext}}^{21} = \left| \frac{S_{\mathrm{ext}}^{21} - S_{\mathrm{num},1}}{S_{\mathrm{ext}}^{21}} \right|, \tag{16}$$

where the extrapolated value is expressed as:

$$S_{\mathrm{ext}}^{21} = \frac{\left(r_{21}^{p_{\mathrm{conv}}} S_{\mathrm{num},1} - S_{\mathrm{num},2} \right)}{\left(r_{21}^{p_{\mathrm{conv}}} - 1 \right)}. \tag{17}$$

In Table 1, the GCI for the measurement with the highest wind velocity is presented, along with several additional values that were obtained through the utilisation of the aforementioned methodology. The GCI for the medium and fine grids was found to be below 1%. The solution was within the asymptotic range of convergence. Although the medium grid was sufficient, the fine grid was selected for the final simulations to ensure maximum numerical precision.

2.7. Material properties, boundary and initial conditions

As illustrated in Tables 2 and 3, the physical properties are assigned to individual surfaces and volumes. The material

Table 1. Results of the study on the independence of results from grid refinement.

Grid type	Fine	Medium	Coarse
Number of elements	1 985 410	829 650	312 240
Grid refinement ratio	1.34	1.39	–
Characteristic cell size, m	0.11	0.15	0.21
Maximum element, m	0.27	0.34	0.42
Layer thickness growth factor	1.2	1.5	1.9
Relative error, %	0.3	0.9	–
Extrapolated relative error, %	0.2	0.5	–
Grid convergence index, %	0.25	0.65	–

Table 2. Physical properties of materials.

	Mineral wool mat	Steel	Reference
Thermal conductivity, W/(m K)	0.0002t+0.033	50	[22]
Density, kg/m³	100	7 800	mat: [23] steel: [22]
Specific heat capacity, J/(kg K)	750	450	[23]

t – arithmetic mean of the flue gas and air temperatures

Table 3. Physical properties of gases – average values for all measurements.

	Flue gas [22]	Air [24,25]
Thermal conductivity, W/(m K)	0.0281	0.0250
Density, kg/m³	0.977	1.225 (at 288.15 K)
Dynamic viscosity, kg/(m s)	1.904×10^{-5}	1.778×10^{-5}
Specific heat capacity, J/(kg K)	1 026	1 041

properties were adopted in accordance with established standards. The properties of gases were obtained from established standards and authoritative publications on air and gas mixtures. Regarding density, different density models were applied to each fluid. Air was modelled as an incompressible ideal gas, where density varies with a local temperature. This approach accurately captures the buoyancy effects around the duct. In contrast, the flue gas was modelled with a constant density.

The initial conditions were established at the inlet to the flue gas duct and the air domain. These conditions included the velocity and temperature, as determined by the experimental study, as well as the turbulence intensity, which was calculated using the equation proposed by Russo and Basse [26]:

$$I = 0.14\mathrm{Re}^{-0.0790}, \tag{18}$$

where I denotes the turbulence intensity. The Reynolds number was determined for the square root of the channel cross-sectional area as a characteristic dimension, in accordance with the recommendation of Duan et al. [19].

Table 4. Inlet initial conditions for all measurement series.

Measurement series	Temperature, K		Velocity, m/s	
	Flue gas	Air	Flue gas	Air
1	363.8	282.0	6.7	2.7
2	365.2	282.2	6.8	3.7
3	366.1	282.3	6.9	3.2
4	362.1	282.5	8.5	2.5
5	364.3	284.5	6.3	2.7
6	364.8	284.3	6.3	3.0
7	364.8	284.1	6.4	1.9
8	364.9	286.0	6.4	1.9
9	364.7	286.4	6.3	3.2
10	363.4	286.3	6.2	4.1

The temperature and velocity values for all measurement series are presented in Table 4. The turbulence intensity for the flue gas is 5% in all cases, while for the air, it varies between 4% and 5%. The hydraulic diameter is 1.413 m for the flue gas and 10.1 m for the air.

The boundary conditions are described in Table 5. The steel duct walls were modelled on both sides of the insulation body using the Shell Conduction option, allowing for heat conduction within the plane of the metal sheets. A no-slip condition was set on the duct walls, as they are fluid-solid interfaces. An adiabatic condition was applied to the cross-sections of the duct walls (duct ends). A constant temperature equal to the air temperature was assumed on the ground and on the building side, while the other side walls of the wind domain were designated as symmetry boundaries.

The flue gas and air inlets were modelled as velocity-inlet, while the outlets were modelled as pressure-outlet. At the pressure-outlets, a zero-pressure gradient was assumed, with the backflow temperature and turbulence parameters set to values

Table 5. Summary of boundary conditions and numerical settings.

Boundary name	Type	Thermal conditions	Momentum conditions
Flue gas inlet	Velocity-inlet	Temperature (Tab. 4)	Velocity (Tab. 4) and turbulence parameters
Flue gas outlet	Pressure-outlet	Backflow: inlet value	Gauge pressure: 0, backflow: inlet value
Duct walls	Wall	Coupled (shell conduction)	No-slip
Duct ends	Wall	Adiabatic	–
Air inlet	Velocity-inlet	Temperature (Tab. 4)	Velocity (Tab. 4) and turbulence parameters
Air outlet	Pressure-outlet	Backflow: inlet value	Gauge pressure: 0, backflow: inlet value
Wind domain, side walls	Symmetry	–	–
Ground / building	Wall	Temperature: air inlet value	No-slip

corresponding to the respective inlet conditions. This was justified because the temperature drop of the flue gas along the investigated part of the insulated duct is minimal, and the ambient air outside maintains a nearly uniform temperature throughout the domain.

2.8. Basic assumptions in numerical modelling

The issue was modelled as a time-steady problem.

Both flue gas and air were treated as incompressible with respect to pressure changes, as the Mach number was below 0.3. Therefore, a pressure-based calculation module was selected.

The calculations were performed in double precision.

A coupled algorithm was used to solve the system of pressure and velocity equations. In order to solve the pressure equation, due to the presence of mixed convection, the PRESTO! (pressure staggering option) discretisation scheme was used, while second-order upwind schemes were used for the remaining equations.

Franke et al. [8] and Celik et al. [20] posit that the residual value resulting from solving the aforementioned equations should be a minimum of 1×10^{-4}, and that this should be reduced further for the purposes of validation. In accordance with the recommendation of Franke et al. [8], the parameter under investigation should be observed simultaneously. If it remains unchanged during successive iterations, the simulation can also be considered convergent. The convergence criterion was established at a residual value of 1×10^{-6}, with a simultaneous heat flux density variability of less than 0.01% in the final 100 iterations.

3. Experimental validation of the numerical model in a real heating plant

3.1. Test methodology

In order to analyse the phenomenon of heat losses from the horizontal flue gas duct of a heating boiler, an existing system located in a municipal heating plant was selected for the purpose of this study. The boiler operating parameters were meticulously monitored at the plant, which demonstrated that the flue gas losses during the experiment ranged from 4 to 5%. The heat source employed was a WR-25 water grate boiler, which was fuelled by hard coal with an average calorific value of 23 MJ/kg. The nominal parameters, in conjunction with the range of values obtained from measurements during the experiment, are presented in Table 6.

Table 6. Characteristics of the WR-25 water-grate boiler: nominal and experimentally obtained values.

	Nominal values	Values during the experiment
Thermal power, MW	32	19 – 24
Efficiency, %	82	73 – 81
Boiler feed water temperature, °C	70	65 – 72
Heating water temperature, °C	150	115 – 128
Flue gas volume downstream of the boiler, m³/h	53 000	23 000 – 47 000



Fig. 4. The examined section of the flue gas duct on a satellite map of the heating plant (own work, based on geoportal.gov.pl).

Figure 4 presents a satellite map of the analysed section of the flue gas duct located downstream of the dust extraction system. The system in question connects to the ducts from the other boilers operating within the plant just before entering the chimney.

In Figure 5, the measurement stations are indicated. The initial measurement station is situated 1.3 m posterior to the elbow. The measurement holes are located at an interval of 7.04 m. In the section of the duct that was analysed, there was an absence of fully developed flow in the cross-section, which can be attributed to the configuration of the duct. Bejan [27] asserts that fully developed turbulent flow occurs after approximately 10 equivalent diameters have passed behind the disturbance. In this case, such a section would have to start after approximately 14 m. The analysed flue gas duct did not contain any such section.

The measurements were taken a few days after the boiler was started up, when thermal equilibrium had been achieved.

Heat flux sensors were utilised to assess heat losses. The components were installed on the bottom and upper walls of the duct, and situated within the cross-section of the measuring opening, with an approximate distance of 60 cm from the duct axis. The installation of the components along the duct axis was rendered infeasible by the presence of metal sheet joints. The sensor was positioned on the side wall in a location exhibiting uniform insulation quality. This location was selected on the ba-

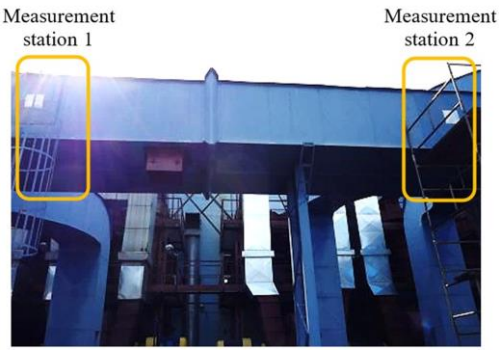


Fig. 5. Measurement stations on the tested section of the duct (own archive).

sis of thermal imaging tests, with the sensor placed at a distance of approximately 60 cm from the measuring station.

The flue gas temperature was measured using PT100 thermometric resistors. During the measurements, the surrounding air humidity was measured using a capacitive humidity probe, and the current weather conditions (cloud cover, precipitation) were recorded. The device was located at the duct support, which was positioned approximately in the middle of the duct section that had been selected for measurement. This section was situated in a location that was sheltered from wind and sun.

The calculations furthermore incorporated the readings of instruments that had been permanently installed in the heating plant, including the mass of coal fed to the boiler, the excess air coefficient, the CO_2 and O_2 content in the flue gas, the flue gas velocity, the wind azimuth and velocity, the ambient air temperature, as well as the air temperature in direct sunlight.

The measurement of air humidity and flue gas temperature was conducted at an interval of 10 s, while the electromotive force measurements from heat flux sensors were recorded at a frequency of 2 min. The readings from the heating plant instruments were recorded as 10-min. averages. The measurement data, which had been prepared for the purpose of validating the numerical model, were grouped into 10-min averages.

3.2. Experimental results and discussion

During the course of the measurements, considerable fluctuations in the heat flux sensor for the upper wall were observed. A rigorous examination of the relationship between the heat flux density on the subject wall and the ambient air temperature in direct sunlight revealed a discernible correlation. Subsequent analysis indicated that this correlation was attributed to the impact of solar radiation, which exhibited a marked intensity that was significantly higher than that observed in other areas. Pearson's correlation coefficient for the heat flux density of the upper wall with the air temperature in direct sunlight was 0.9. Consequently, the outcomes derived from the bottom and side walls (Pearson's coefficients of 0.6 and 0.1, respectively) were selected for validation.

The measurement series were analysed in terms of wind pressure on the duct. The location of the heating plant building is such that it is in close proximity to the duct. The building functions as a barrier to south and west winds. The wind velocity value was obtained from the heating plant's instruments; consequently, it was not measured exactly at the duct location. Following the consideration of wind azimuth readings, as determined by the data measured at the heating plant, the validation was conducted exclusively on those measurements during which the wind was not blowing from the direction of the building.

Figure 6 shows the results of the heat flux density measurements together with the total uncertainty bars. The graph also shows the values of ambient air temperature, air temperature in direct sunlight, wind velocity and the temperature difference between the flue gas and the air. The values are connected by lines to make the profiles of the variables easier to read. During measurements, the heat losses obtained from the bottom wall ranged from 28 to 37 W/m^2, and from 29 to 44 W/m^2 from the side wall. In each measurement series, the total uncertainty of the heat flux

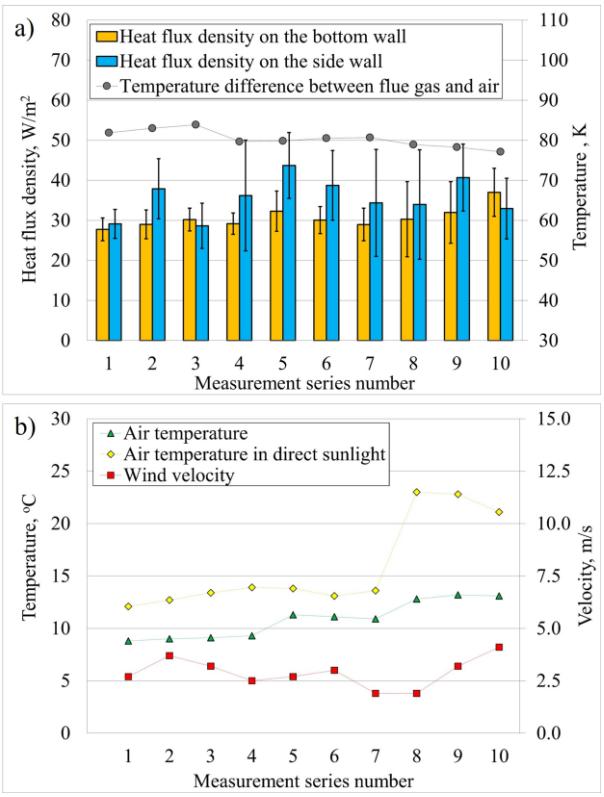


Fig. 6. Experimental results for heat flux density (a) and weather parameters (b).

density from the bottom wall was lower than that of the side wall. For the bottom wall, the total measurement uncertainty is clearly greater where solar radiation heats the flue gas duct walls intensively.

The obtained heat flux density profiles show a negative correlation with the temperature difference between the flue gases and the air. This is due to the simultaneous influence of weather phenomena, such as solar radiation and wind velocity, on the temperature of the duct wall (Pearson's coefficient is –0.7 for the bottom wall and –0.4 for the side wall). The measured electromotive force increases as the temperature of the duct wall increases. This temperature increase is due not only to the temperature difference between the media on both sides of the wall, but also to solar radiation and conduction of absorbed heat along the wall. The incorrect correlation is clearly visible in measurements 8–10. During these measurements, a significant rise in heat losses was observed despite a decrease in the temperature difference between the flue gas and the air. This decrease should result in decreased heat losses, yet a negative Pearson coefficient was obtained.

As shown above, measuring heat losses with heat flux sensors, which have the advantage of not requiring significant interference with the existing installation, is also subject to considerable uncertainty due to current weather conditions, particularly those resulting from the intensity of solar radiation and wind gusts. Nevertheless, bearing these limitations in mind and accounting for measurement uncertainty, the test results were used to validate the numerical model of heat exchange in the heating plant's flue gas duct.

4. Simulation results and model validation

All simulations were considered to have converged because the behaviour equations reached the assumed residual value, and the heat flux density stabilised below 0.01% in at least the last 100 iterations in all simulations.

Figure 7 shows the results of the numerical simulation compared with the results of the experimental study, together with the total uncertainty. In the case of the bottom wall, the measuring sensor was mounted approximately 60 cm from the duct axis in the windward direction, while the simulation result includes the average heat flux density across the entire surface.

The consistency of the numerical calculations with the experimental data was analysed using two methods. The first

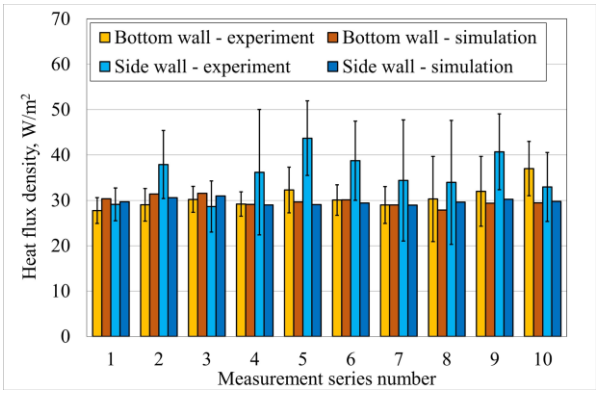


Fig. 7. Comparison of simulation and experimental results.

method leads to the determination of the key validation metric, U_V. This method was described by Stern et al. [22], for example. It takes into account errors and uncertainties in both data categories to assess the level of validation. The second method is used when there is insufficient data to calculate the aforementioned errors and uncertainties, and it calculates the relative coefficient of variation of the root mean square error CV(RMSE). This method was employed to compare the results with those in the literature, even though the data were available. No publications describing the validation of numerical models by an experiment conducted in the presence of variable weather conditions based on the first method were found. The second method, on the other hand, is used in publications concerning the validation of analyses of phenomena on external building elements.

In the method used to determine the validation metric U_V, the comparison error E should not exceed the metric itself, indicating good agreement between the results obtained in the numerical simulation and the experiment on the actual object:

$$E = |\bar{D} - S_{\text{num}}|, \tag{19}$$

$$U_V{}^2 = U_D{}^2 + U_{SPD}{}^2 + U_{SN}{}^2, \tag{20}$$

where: E – comparison error, $\bar{D}$ – mean measured value, U_V – process validation metric, U_D – uncertainty of experimental values, U_{SPD} – uncertainty due to input data (e.g. material data), U_{SN} – uncertainty of numerical simulation.

The uncertainty of the values obtained in the experiment (U_D) was taken as the expanded uncertainty according to Eqs. (21)–(25). The confidence level p was taken to be 95%, and the number of degrees of freedom was taken to be 4. Therefore, the Student's t-distribution critical value was 2.7765.

$$U_D = t_p(\nu_{\text{dof}})u_{c,i}, \tag{21}$$

$$\nu_{\text{dof}} = n - 1, \tag{22}$$

$$u_{c,i} = \sqrt{u_a^2 + u_b^2}, \tag{23}$$

$$u_a = \frac{s}{\sqrt{n}}, \tag{24}$$

$$s = \sqrt{\frac{1}{n-1}\sum_{i=1}^{n}[D_i - \bar{D}]^2}, \tag{25}$$

where: $t_p(\nu_{\text{dof}})$ – Student's t-distribution coefficient for confidence level p and degrees of freedom ν_{dof}, $u_{c,i}$ – combined standard uncertainty for measurement number i, n – number of measurements in a series, u_a – type A standard uncertainty, u_b – systematic standard uncertainty, s – standard deviation, D_i – i-th measured value.

Errors resulting from the use of the input data (U_{SPD}) were determined based on the assumption that heat losses mainly depend on the temperature difference between flue gas and air, as well as the insulation thickness and thermal conductivity coefficient. According to Żarnowski and Wiśniewski [29], the thermal conductivity coefficient of mineral wool insulation does not change significantly over time; therefore, this parameter was omitted in the analysis of uncertainties resulting from the use of input data. The heat flux density is directly proportional to the temperature difference between the flue gases and the air, and inversely proportional to the thickness of the insulation:

$$Q \sim \frac{\Delta T}{\delta}, \tag{26}$$

where: ΔT – temperature difference between flue gas and air, δ – insulation thickness.

The uncertainty in the insulation thickness was assumed to be 3%, due to settlement, in accordance with the results of the study by Nagy et al. [30]. In the absence of measurement uncertainty for the air temperature, which was measured by devices permanently installed in the heating plant, the total uncertainties of the temperature difference were determined only on the basis of the systematic and random errors of the flue gas temperature measurements. A value of approximately 1% was obtained for all measurements. The total uncertainty of the heat flux density resulting from the use of input data was determined in accordance with the law of uncertainty propagation, assuming a linear relationship between the temperature difference, insulation thickness and heat losses.

The GCI obtained in the grid independence analysis was adopted as the uncertainty of the numerical simulation (U_{SN}).

When analysing the compliance of the numerical simulation results with the measurement data, a second method was employed to determine CV(RMSE) according to the following equations:

$$\mathrm{CV(RMSE)} = \frac{\mathrm{RMSE}}{\bar{D}} 100, \tag{27}$$

$$\mathrm{RMSE} = \sqrt{\frac{1}{n}\sum_{i=1}^{n}(S_{\mathrm{num}} - D_i)^2}, \tag{28}$$

where: CV(RMSE) – relative root mean square error, RMSE – root mean square error, i – measurement number in a single measurement series, n – number of measurements in a single measurement series.

The validation results are presented in Fig. 8. With the exception of measurements 4 and 6 for the side wall, the comparison error E does not exceed the validation metric U_V, proving that the numerical simulation results are consistent with the measurements within the accepted uncertainty limits. CV(RMSE) ranged from 7% to 22% for the bottom wall and from 9% to 36% for the side wall. These high percentage values result from the low absolute value of the measured heat flux and the variability of weather conditions during the experiment, which were averaged for each 10-min measurement series. Similar levels can be found in the literature. For example, Demanega et al. [31] calculated CV(RMSE) for heat losses from a building's window surface. The measurements were taken on cloudless days using heat flux sensors. Depending on the numerical model selected, the relative root mean square error ranged from 16% to 38%.

Figure 9 shows the heat flux density distributions across the bottom and side walls of the duct. It should be noted that the extreme values observed during the experiment do not coincide with the numerical extremes (see Fig. 7). Therefore, Fig. 9 presents the simulation results for the bottom wall measurement series, corresponding to both the numerical and experimental extremes (the latter being intermediate in the simulation). For all illustrated series, heat flux density on the bottom wall on the windward side is significantly lower. Regarding the side wall, a single simulation result is presented (for the series with the highest experimental heat flux density), which is sufficient to demonstrate that the heat flux density is distributed more evenly along its surface. The characteristic profile shape on the bottom wall remains consistent regardless of the heat flux density magnitude (covering maximum, minimum and intermediate values). It confirms the robustness of the model in reproducibly capturing the heat transfer patterns across all measurement series.

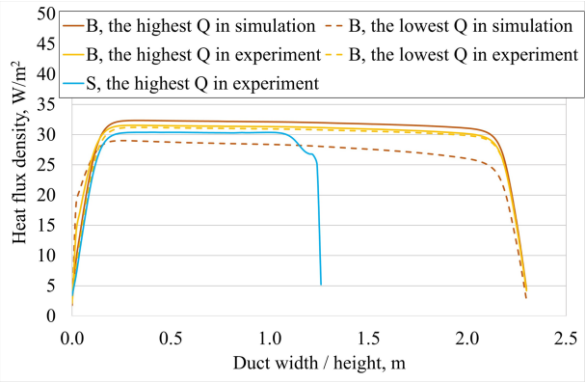


Fig. 9. Heat flux density (Q) across the bottom (B) and side (S) wall of the duct (wind reversal on the bottom wall opposite to the horizontal axis reversal).

The heat flux density distributions illustrate the result from the velocity field and wind streamlines shown in Fig. 10. After flowing into a channel-shaped obstacle, the air stream separates and changes direction, forming vortices that lead to a local decrease in convection intensity. In turn, the intensity of convection affects the air temperature around the duct, the field of which is presented in Fig. 11. Both figures refer to the series with the highest heat flux density, which was obtained in simulations on the bottom wall.

The nature of the wind flow described affects the variation in heat losses on the surface of individual walls and between them. Figure 12 illustrates the temperature field on the outer sur-

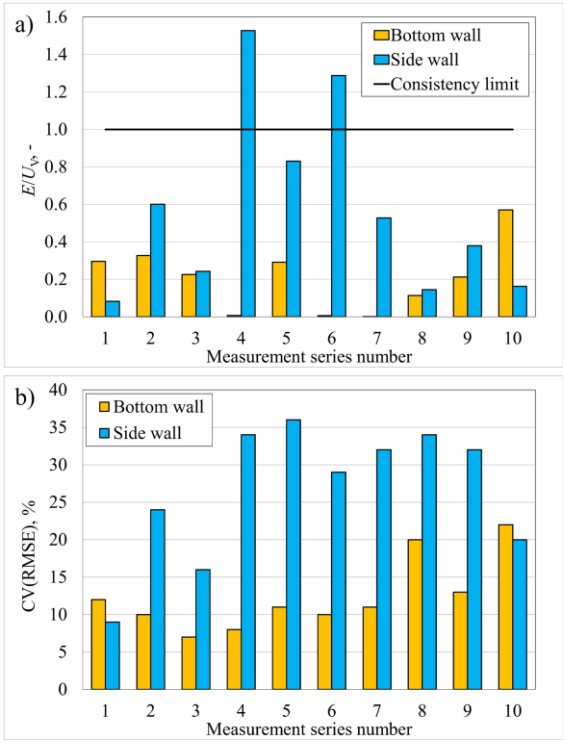


Fig. 8. Validation consistency: a) validation metric (E/U_v), and b) relative root mean square error (CV(RMSE)).

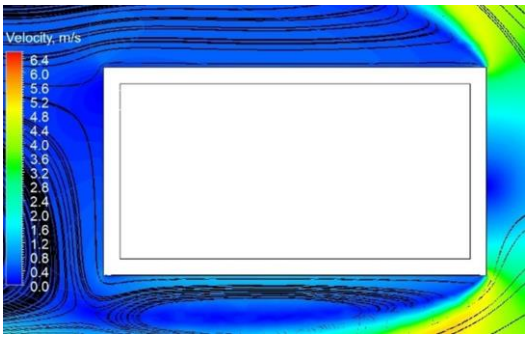


Fig. 10. Velocity field and air flow streamlines around the duct; right side of the illustration corresponds to the windward side (ANSYS CFD-Post 2024 R2).

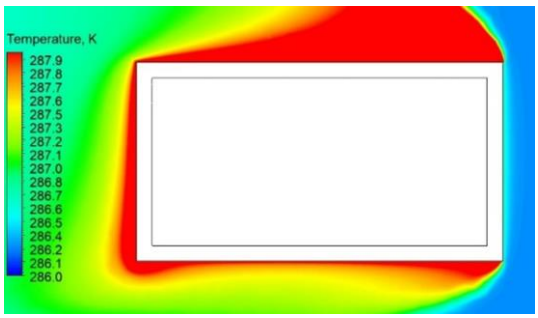


Fig. 11. Air temperature field around the duct; right side of the illustration corresponds to the windward side (ANSYS CFD-Post 2024 R2).

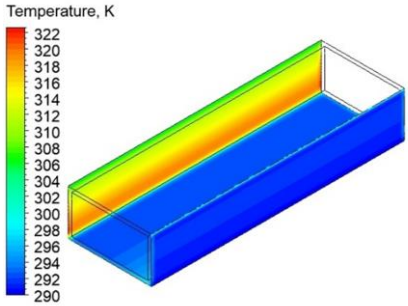


Fig. 12. Temperature field on the duct walls; right side of the illustration corresponds to the windward side (ANSYS CFD-Post 2024 R2).

faces of the bottom and side walls. As can be seen from the difference in surface temperature, heat losses on the leeward side of the side walls are lower than on the windward side. The side walls follow the typical trend of lower temperatures on the windward side. For the bottom wall, the temperature is higher on the windward side than on the leeward side. This phenomenon is attributed to the separation of the air stream at the leading edge and the formation of local flow disturbances, which reduce local heat transfer efficiency despite the windward orientation.

Figure 13 shows the temperature field in the flue gas duct insulation. On the windward and bottom sides of the duct, the temperature of the insulation in contact with the outside air is significantly lower than on the top wall and leeward side.



Fig. 13. Temperature field in the duct insulation; right side of the illustration corresponds to the windward side (ANSYS CFD-Post 2024 R2).

5. Summary and conclusions

The article describes the process of validating a numerical model of the heat exchange between the flue gas flowing through the horizontal, rectangular duct of a heating plant and the surrounding air. The model considers the effects of wind and solar radiation. The computational domain includes both the duct and the surrounding airspace. This was defined based on guidelines for numerical simulations for buildings.

The validation experiment was conducted under variable weather conditions, including cloud cover, air temperature and wind velocity.

Validation was carried out for the bottom and side walls of the duct. This was analysed in two ways. The uncertainty-based method showed that, for almost all measurement series, the comparison error did not exceed the validation metric. In contrast, the second method, which did not take uncertainty into account, produced fairly high values of the relative mean square error coefficient: up to 22% for the bottom wall and 36% for the side wall. However, these values are comparable to those reported in the literature, describing the experimental validation of models of external building elements exposed to rapidly changing weather conditions. It should be noted that heat losses measured with heat flux sensors are subject to high error due to rapidly changing intensity of solar radiation, wind velocity and wind direction. Nevertheless, they are a research tool that interferes very little with the existing installation.

The results obtained indicate that the developed numerical model can be used to analyse flue gas duct modernisation in order to reduce heat losses from flue gases flowing through the duct in terms of the bottom and side walls. These analyses may include the actual sunlight conditions, as well as the wind velocity and temperatures at a given location.

To summarise, the following specific conclusions were drawn from the research:

– the upper wall was excluded from the validation process due to extreme heat flux fluctuations caused by direct solar exposure. A very high Pearson correlation coefficient (0.9) between the heat flux density and air temperature in direct sunlight confirmed that solar radiation dominated the thermal signal, making these measurements unsuitable for reliable numerical comparison;
– the validation showed a significantly higher discrepancy for the side walls compared to the bottom wall. This is attributed to the high sensitivity of heat flux sensors to rapid solar radiation changes, which introduces measurement uncertainty that affects the final validation results for those surfaces;
– the numerical model, utilising the k–ω SST turbulence model, correctly captured the well-known phenomenon of flow separation at the leading edge of the duct. The resulting vortices explain the specific heat flux density profile on the bottom wall observed in the simulations;
– the numerical model demonstrated robustness, as the characteristic shape of the heat flux density profile on the bottom wall remained consistent across measurement series,

regardless of the heat flux density magnitude. This confirms that the model reproducibly captures the underlying heat transfer patterns under boundary conditions observed during the experiment.

The study leads to the following general conclusions:

– the use of heat flux sensors, while subject to environmental interference, is a non-invasive diagnostic method for large-scale energy systems where operational continuity is required;
– the application of an uncertainty-based validation approach (based on the E/U_V ratio) is recommended for evaluating industrial models in uncontrolled environments (changing weather conditions), as it provides a more objective measure of accuracy than the standard error coefficient CV(RMSE), by accounting for experimental uncertainty;
– the developed numerical model offers an important step towards making thermal insulation of ducts in district heating infrastructure adaptable to individual location and environmental conditions.

References

[1] Statistics Poland. (2026). *Energy consumption in households in 2024*. Statistics Poland; Statistical Office in Rzeszów (in Polish).

[2] Department of Electricity and Heat Markets of the Energy Regulatory Office (ERO) in cooperation with the ERO Branch Offices. (2025). *Heat energy in figures – 2024*. Energy Regulatory Office (in Polish).

[3] Zhang, Q., Yi, H., Yu, Z., Gao, J., Wang, X., Linc, H., & Shen, B. (2018). Energy-exergy analysis and energy efficiency improvement of coal-fired industrial boilers based on thermal test data. *Applied Thermal Engineering*, 144, 614–627. doi: 10.1016/j.applthermaleng.2018.08.069

[4] Matas, R., Kňourek, J., & Novák, M. (2024). Analysis and validation of CFD simulations for flow in the large power station flue gas system. *EPJ Web of Conferences*, 299, 01025. doi: 10.1051/epjconf/202429901025

[5] Chen, G.Y., Yuan, G.D., Zheng, L.Y., Guo, X.K., Lv, A.L., Geng, Y., Cui, Z.Z., Long, H., Yan, B.B., Ni, Y., & Long, Z.W. (2013). Analysis of flow in power plant flue via Fluent simulations. *Advanced Materials Research*, 838–841, 2630–2633. doi: 10.4028/www.scientific.net/AMR.838-841. 2630

[6] El-Shafie, M. (2022). Theoretical and experimental analysis of temperature decay along an industrial chimney using analytical and k-ω turbulence models. *Case Studies in Chemical and Environmental Engineering*, 6, 100264. doi: 10.1016/j.cscee.2022.100264

[7] Huang, W., Xu, Q., Zhao, B., Lv, Q., & Wang, G. (2025). Urban multi-scale building energy modelling (BEM) and computational fluid dynamics (CFD) integration: Tools, strategies and accuracy for energy microclimate analysis. *Journal of Building Engineering*, 103, 112041. doi: 10.1016/j.jobe.2025.112041

[8] Franke, J., Hellsten, A., Schlünzen, H., & Carissimo, B. (2007). *Best practice guideline for the CFD simulation of flows in the urban environment*. COST Action 732: Quality Assurance and Improvement of Microscale Meteorological Models.

[9] Tominaga, Y., Mochida, A., Yoshie, R., Kataoka, H., Nozue, T., Yoshikawa, M., & Shirasawa, T. (2008). AIJ guidelines for practical applications of CFD to pedestrian wind environment around buildings. *Journal of Wind Engineering and Industrial Aerodynamics*, 96(10–11), 1749–1761. doi: 10.1016/j.jweia.2008.02.058

[10] Bejan, A. (2013). External natural convection. In *Convection heat transfer* (pp. 168–232). Wiley.

[11] Hamisu, M.T., Jamil, M.M., Umar, S.U., Sa'ad, A. (2019). Numerical study of flow in asymmetric 2D plane diffusers with different inlet channel lengths. *CFD Letters*, 11(5), 1–21.

[12] Menter, F.R. (1994). Two-equation eddy-viscosity turbulence models for engineering applications. *AIAA Journal*, 32(8), 1598–160521. doi: 10.2514/3.12149

[13] Ansys. (2024). *Ansys Fluent Theory Guide* (Release 2024 R2). Ansys, Inc.

[14] Carvalho, H.D.R., Chang, B., McInnes, K.J., Heilman, J.L., Wherley, B., & Aitkenhead-Peterson, J.A. (2021). Energy balance and temperature regime of different materials used in urban landscaping. *Urban Climate*, 37, 100854. doi: 10.1016/j.uclim.2021.100854

[15] Yu, B., Chen, Z., Shang, P. & Yang, J. (2008). Study on the influence of albedo on building heat environment in a year-round. *Energy and Buildings*, 40(5), 945–951. doi: 10.1016/j.enbuild.2007.07.009

[16] Liu, H., Chen, Z., Chen, B., Xiao, X. & Wang, X. (2014). Studies on the temperature distribution of steel plates with different paints under solar radiation. *Applied Thermal Engineering*, 71(1), 342–354. doi: 10.1016/j.applthermaleng.2014.06.031

[17] Bergman, T.L. & Lavine, A.S. (2017). *Fundamentals of Heat and Mass Transfer* (8th ed.). Wiley.

[18] Schlichting, H., & Gersten, K. (2017). Fundamentals of boundary–layer theory. In *Boundary-Layer Theory* (pp. 29–49). Springer. doi: 10.1007/978-3-662-52919-5

[19] Duan, Z., Yovanovich, M.M., & Muzychka, Y.S. (2012). Pressure drop for fully developed turbulent flow in circular and noncircular ducts. *Journal of Fluids Engineering*, 134(6), 061201. doi: 10.1115/1.4006861

[20] Celik, I.B., Ghia, U., Roache, P.J., Freitas, C.J., Coleman, H., & Raad, P.E. (2008). Procedure for estimating and reporting uncertainty in s due to discretisation in CFD applications. *Journal of Fluids Engineering*, 130(7), 078001. doi: 10.1115/1.2960953

[21] Roache, P.J. (1994). Perspective: A method for uniform reporting of grid refinement studies. *Journal of Fluids Engineering*, 116(3), 405–413. doi: 10.1115/1.2910291

[22] Polski Komitet Normalizacyjny. (2019). *PN-EN 13384-1+A1: 2019-07. Chimneys – Methods for thermal and flow calculations – Part 1: Chimneys connected to a single heating appliance*. PKN (in Polish).

[23] Polski Komitet Normalizacyjny. (2004). *PN-EN 13384-1:2004. Chimneys – Methods of thermal and flow calculations – Part 1: Chimneys connected to a single furnace*. PKN (in Polish).

[24] Kruczek, S. (2001). *Boilers. Designs and calculations*. Oficyna Wydawnicza Politechniki Wrocławskiej (in Polish).

[25] Oleśkowicz-Popiel, C., & Wojtkowiak, J. (1997). Formulas approximating the physical properties of air. *Ciepłownictwo, Ogrzewnictwo, Wentylacja*, 28(3), 324 (in Polish).

[26] Russo, F., & Basse, N.T. (2016). Scaling of turbulence intensity for low-speed flow in smooth pipes. *Flow Measurement and Instrumentation*, 52, 101–114. doi: 10.1016/j.flowmeasinst.2016.09.012

[27] Bejan, A. (2013). Turbulent duct flow. In *Convection heat transfer* (pp. 369–397). Wiley.

[28] Stern, F., Wilson, V.R., Coleman, W.H., & Paterson, G.E. (2001). Comprehensive approach to verification and validation of CFD simulations—Part 1: Methodology and procedures. *Journal of Fluids Engineering*, 123(4), 792–802. doi: 10.1115/1.1412235

[29] Żarnowski, T., & Wiśniewski, T. (2014). Ageing of fibrous insulation used in heating and power engineering. *Instal*, 12, 21–27 (in Polish).

[30] Nagy, B., Nemes, R., & Simon, T. (2020). Effect of built-in mineral wool insulation durability on its thermal and mechanical performance. *Journal of Thermal Analysis and Calorimetry,* 139, 169–181. doi: 10.1007/s10973-019-08384-5

[31] Demanega, I., De Michele, G., Pernigotto, G., Gasparella, A., & Avesani, S. (2023). Development and experimental validation of a CFD model for the thermal behaviour assessment of complex fenestration systems. *Journal of Building Engineering,* 68, 106150. doi: 10.1016/j.jobe.2023.106150